SPATIAL CHAOS, BREATHERS AND PHONOBREATHERS IN A PINNED MECHANICAL LATTICE

S.C.GREEN[†‡], C.J.BUDD[†‡¶], AND G.W.HUNT[†§]

Abstract. We present an overview of the static and some of the dynamic behaviour of a finite, pinned lattice system of interest in structural mechanics. We see that of all the many static equilibrium states that can be found a few may be observed in an experiment. We then go onto show that this mechanical lattice can support linearly stable breather solutions which have a lifetime in the nonlinear lattice of at least 20 breather periods. Finally we show how this breather solution bifurcates to produce phonobreather solutions. After seeing that the frequency of a phonobreather solution does not depend on its amplitude, the nonlinear stability of this phonobreather is investigated and it is found that the phonobreather core's width grows at a constant velocity. We conclude that both breather and phonobreather solutions are potentially observable in an experiment on this mechanical lattice.

Key words. Mechanical lattice, Hamiltonian lattice, iterated map, discrete boundary value problem, spatial chaos, dynamics, discrete breathers, phonobreathers

AMS subject classifications. 00A06 34K13 34K23 70C20 70E50 70E55 70H12 70J50 70K42

1. Introduction. Pinned and linked mechanical systems of the form illustrated in Figure 1.1 as well as being of great importance in structural engineering [11] have remarkably rich static [7] and dynamic behaviour. This can include spatially chaotic stationary solutions as well as a wide range of localised time varying 'breathers'. The purpose of this paper is to describe and analyse these behaviours and to consider their physical relevance. A mathematical model for such systems with fixed lattice boundaries ($Q_0 = Q_N = 0$), derived in detail in §2, is of the form

$$H = \sum_{i=1}^{N-1} \frac{m}{2}\dot{Q}_i^2 + \sum_{i=1}^{N-1} \frac{k}{2}Q_i^2 + Ph \sum_{i=1}^{N-1} \sqrt{1 - \left(\frac{Q_{i+1} - Q_i}{h}\right)^2} \tag{1.1}$$

which combines the kinetic energy, the potential energy stored in the springs and the work done by the axial load in shortening the system.

We first consider the static equilibrium (or zero frequency) states of this system and find that for $h < 4P/k$ the spatial behaviour is quite regular, but for $h > 4P/k$ a large number of spatially irregular solutions appear (e.g. see Figure 3.4) which clearly demonstrates the effects of coarse graining in the system. These results are found by searching for fixed points of the above Hamiltonian dynamical system using a discrete boundary value problem (BVP) constructed from a symplectic map $\phi : \mathbb{R}^2 \to \mathbb{R}^2$. The above explosion of solutions corresponds to the appearance of a Homoclinic tangle in the phase space of the map ϕ for $h > 4P/k$. Similar results are found in [7], however we consider a different mechanical system which does not allow overlap in the plane of movement which we believe is more structurally relevant. We also consider how these solutions will affect experimental behaviour and analyse their dynamic stability.

These mechanically derived systems also arise naturally when a semi-discrete numerical method (continuous in time, discrete in space) is used to discretise certain PDEs. In this case $h > 0$ corresponds to the *spatial step-size*. Previously, the multitude of static solutions mentioned above

[†]Centre for Nonlinear Mechanics, University of Bath, Bath, BA2 7AY, UK
[‡]Department of Mathematical Sciences
[§]Department of Mechanical Engineering
[¶]Corresponding author; mascjb@bath.ac.uk

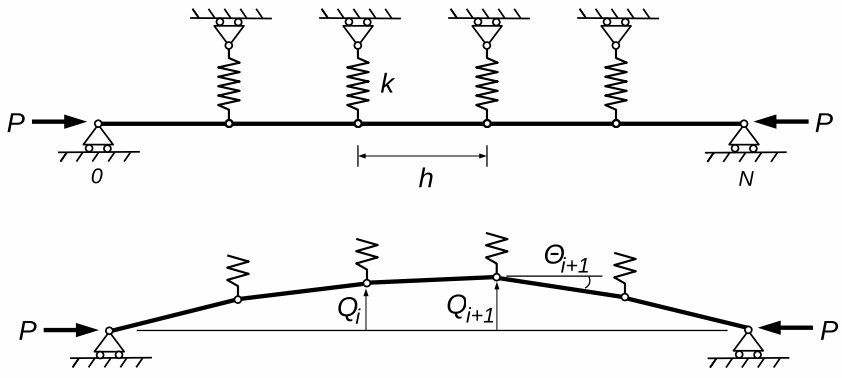

FIG. 1.1. *The mechanical system in its flat state (top) and a displaced state (bottom) from [11] that will be studied in this article. It consists of a chain of freely pin jointed rigid links of length $h > 0$ constrained to lie in a plane. The vertical springs are linear and the system is axially loaded by a force P at the end points.*

were seen as spurious or parasitic ([4] and references therein) but in this paper we demonstrate that the solutions to these discrete BVPs are physically interesting in their own right. For comparison we show the continuum limit of this discrete mechanical system and see that in the continuum system the lowest buckling load gives an unphysical, infinitely wrinkled, zero wavelength static solution and that, contrastingly, the discreteness of the pin jointed mechanical system gives a primary buckled solution with a non-zero wavelength.

The complex behaviour of the static equilibrium states of this lattice inevitably leads us to expect interesting dynamic behaviour; we are not disappointed. One type of periodic nonlinear lattice behaviour that has received a lot of attention in recent times is that of breather solutions (for reviews see [8, 1, 2]). Breather solutions are time periodic solutions that are localised in space. Despite the many publications few of the applications have been from macroscopic engineering systems. Localisation of energy in these systems can have catastrophic consequences, for instance excessive vibration of a single turbine blade leading to premature failure, or vibration concentration in the lattice of a steel building causing excessive fatigue.

There are proofs of the existence of breather solutions in quite general lattice equations with linear coupling [15] or nonlinear coupling and hardening potentials [13, 3]. In the mechanical system we study the only nonlinearity is a softening nearest neighbour coupling and so it is necessary to use numerical methods to demonstrate the existence of breathers. One method for doing this is that of Marin and Aubry [16]. These calculations indicate that the mechanical system admits breathers if h is large enough and that the breathers located are linearly stable and have a long lifetime (at least 20 breather periods) in the fully nonlinear lattice. Hence this behaviour is potentially observable in an experiment.

Since the first breather existence proof of MacKay and Aubry in 1994 [15] there has been a huge amount of interest in the mathematical study and experimental observation of these solutions. At around this time solutions called phonobreathers which appear to be a superposition of a nonlinear phonon with a breather solution were also discovered [16] in lattices with nonlinear on-site terms. Since then there has been little interest in these solutions and only more recently have they been investigated further [18]. In this paper we demonstrate further that the mechanical lattice (with

coupling nonlinearity only) can also support phonobreather solutions. Moreover, we demonstrate that the nonlinear dynamics close to a phonobreather solution is sufficiently recurrent to enable the experimental observation of this behaviour. This recurrent behaviour takes the form of a slowly growing phonobreather core that expands at a constant velocity slowly enveloping the nonlinear phonon tails and can be seen in the movie file 'pb1drift.mpg' that accompanies this paper on-line.

The layout of this paper is as follows. In §2 we introduce the mechanical model of [11] and the assumptions we are making in modelling the dynamic behaviour of this system before deriving the Hamiltonian system (1.1). In §3 we show how we look for static equilibrium states in this model using a discrete BVP and then describe the complex behaviour of this BVP. This section concludes with a prediction of the behaviour of an experiment performed under controlled end shortening conditions before the stability of the static equilibrium solutions under controlled load is presented in §4. Section 5 starts with a brief summary of the method of [16] on how to find breathers in nonlinear lattices before we do just that for our mechanical system. A short demonstration of the linear and nonlinear stability of a breather solution in this lattice confirms that we expect to be able to observe these experimentally. Finally we show how a breather solution can bifurcate to give phonobreather solutions and then present new results on the nonlinear dynamics near to this phonobreather trajectory. In conclusion we relate the calculated static and dynamic behaviour to observable mechanical phenomena.

2. Modelling. The mechanical system we consider in this paper is that of [11] and is shown in Figure 1.1. It consists of a freely pin jointed structure with N, mass-less, rigid links of length $h > 0$. The displacements Q_i, for $i = 0, \ldots, N$, of the joints (mass m) are constrained to lie in the same plane and the system is constrained at the ends so that $Q_0 = Q_N = 0$. The system is also subject to a steady axial load P. We can write the potential energy of this system V in terms of the energy stored in the springs U and the work done my P in producing a total end shortening $\mathcal{E}$ where

$$\mathcal{E} = h \sum_{i=0}^{N-1} \left(1 - \sqrt{1 - \left(\frac{Q_{i+1} - Q_i}{h} \right)^2} \right). \tag{2.1}$$

After neglecting constant terms V is written

$$V = U - P\mathcal{E} = \tfrac{1}{2} k \sum_{i=0}^{N} Q_i^2 + Ph \sum_{i=0}^{N-1} \sqrt{1 - \left(\frac{Q_{i+1} - Q_i}{h} \right)^2}. \tag{2.2}$$

We note here that we are working with displacements of the lattice that satisfy $\Theta_i \in (-\frac{\pi}{2}, \frac{\pi}{2})$ and so $|Q_{i+1} - Q_i| < h$. In this potential energy expression we have included the full geometric nonlinearity which will allow us later to explore the full global bifurcation diagram for the static equilibrium states. In order to make the dynamic analysis tractable we use the small displacement approximation to the kinetic energy of the system given by

$$T = \sum_{i=1}^{N-1} \frac{m}{2} \dot{Q}_i^2 + \mathcal{O}(Q^4). \tag{2.3}$$

Using (2.2) and (2.3) we can write down the Lagrangian $\mathcal{L}$ for this system

$$\mathcal{L} = T - V = \sum_{i=1}^{N-1} \frac{m}{2} \dot{Q}_i^2 - \tfrac{1}{2} k \sum_{i=0}^{N} Q_i^2 - Ph \sum_{i=0}^{N-1} \sqrt{1 - \left(\frac{Q_{i+1} - Q_i}{h} \right)^2}, \tag{2.4}$$

with $Q_0 = Q_N = 0$ and Hamiltonian given by 1.1. It is convenient to nondimensionalise this using the following scalings

$$h = L\delta, \quad Q_i = LU_i, \quad \lambda = \frac{kL^2}{Ph} = \frac{kL}{P\delta}, \quad t = \sqrt{\frac{mL}{P\delta}}\bar{t} = \sqrt{\frac{m}{k}}\lambda\bar{t} \tag{2.5}$$

where $L = Nh$ and so $\delta = 1/N$. These give the scaled Lagrangian we study in this article

$$\mathcal{L}(\mathbf{U}, \dot{\mathbf{U}}) = \sum_{i=1}^{N} \left(\tfrac{1}{2}\dot{U}_i^2 - \tfrac{1}{2}\lambda U_i^2 \right) - \sum_{i=1}^{N-1} \sqrt{1 - \left(\frac{U_{i+1} - U_i}{\delta} \right)^2} \tag{2.6}$$

where we have used $\mathbf{U} = (U_1, U_2, \ldots, U_{N-1})$ and the corresponding scaled Hamiltonian is given by

$$H = \sum_{i=1}^{N-1} \tfrac{1}{2}\dot{U}_i^2 + \sum_{i=1}^{N-1} \tfrac{1}{2}\lambda U_i^2 + \sum_{i=1}^{N-1} \sqrt{1 - \left(\frac{U_{i+1} - U_i}{h} \right)^2}$$

The equations of motion for this Hamiltonian can then be written in the form

$$\dot{\mathbf{X}} = \mathbf{F}(\mathbf{X}) \equiv \begin{pmatrix} \dot{\mathbf{U}} \\ \mathbf{f}(\mathbf{U}) \end{pmatrix} \tag{2.7}$$

where $\mathbf{X} = (U_1, U_2, \ldots, U_{N-1}, \dot{U}_1, \ldots, \dot{U}_{N-1})^{\mathrm{T}}$ and

$$\mathbf{f}(\mathbf{U}) = \begin{pmatrix} -\lambda U_1 - \frac{1}{\delta}\bar{g}\left(\frac{U_2 - U_1}{\delta}\right) + \frac{1}{\delta}\bar{g}\left(\frac{U_1}{\delta}\right) \\ \vdots \\ -\lambda U_i - \frac{1}{\delta}\bar{g}\left(\frac{U_{i+1} - U_i}{\delta}\right) + \frac{1}{\delta}\bar{g}\left(\frac{U_i - U_{i-1}}{\delta}\right) \\ \vdots \\ -\lambda U_{N-1} - \frac{1}{\delta}\bar{g}\left(\frac{-U_{N-1}}{\delta}\right) + \frac{1}{\delta}\bar{g}\left(\frac{U_{N-1} - U_{N-2}}{\delta}\right) \end{pmatrix} \tag{2.8}$$

with $\bar{g}(x) = x/\sqrt{1 - x^2}$. This system has two free parameters λ and N. We have nondimensionalised these expressions in a form that makes the continuum limit clear in the next section. The cost of this is that we have a dependent parameter $\delta = 1/N$ in the equations of motion and that the parameter λ is reciprocally related to the physical load P. These issues can be rectified by using a scaling symmetry of this system to regroup the variables and parameters. If we let $p = 4/(\lambda\delta^2)$ be the nondimensional load and consider the groups U_i/δ and $\sqrt{\lambda}t$ we find that δ scales out of our equations of motion and $p \propto P$. We will later use both of these scalings as convenient.

3. Static Equilibrium States. In this section we investigate the behaviour of the static equilibrium states of the mechanical system of Figure 1.1 using similar methods to those used in [7]. In particular, we rewrite the vector equation $\mathbf{f}(\mathbf{U}) = 0$ to give a discrete boundary value problem formed from a two dimensional area preserving map. To derive this map and ensure it inherits the global symmetry properties of the mechanical system we, however, use the theory of discrete mechanics [17]. To do this we first set $\dot{U}_i = 0$ for all i and rewrite (2.6) in the form

$$-\delta\mathcal{L}(\mathbf{U}, \mathbf{0}) \equiv S_\beta(\mathbf{U}) = \sum_{i=0}^{N-1} L_d^\beta(U_i, U_{i+1}) + \frac{\delta\lambda}{2}\left(\beta Q_0^2 + (1-\beta)Q_N^2\right)$$

where

$$\mathcal{L}_d^\beta(U_i, U_{i+1}) = \frac{\lambda\delta}{2}\left(\beta U_{i+1}^2 + (1-\beta)U_i^2\right) + \delta\sqrt{1-\left(\frac{U_{i+1}-U_i}{\delta}\right)^2}.$$

In this expression there is a free parameter β which determines at which end of the lattice the remainder terms for the sum occur. We will choose the value of β appropriately later. As described in [17] we can use the condition that $S_\beta(\mathbf{U})$ is stationary with respect to $\mathbf{U}$ to derive an area preserving map $\phi^\beta : \mathbb{R}^2 \to \mathbb{R}^2$ and a corresponding discrete BVP that gives the static equilibrium states of the mechanical system. This map is given by

$$\phi^\beta : \begin{pmatrix} U_i \\ W_i \end{pmatrix} \to \begin{pmatrix} U_i - \delta\frac{W_i+(1-\beta)\delta\lambda U_i}{\sqrt{1+(W_i+(1-\beta)\delta\lambda U_i)^2}} \\ W_i + \delta\lambda((1-\beta)U_i + \beta U_{i+1}) \end{pmatrix} \tag{3.1}$$

where $W_i = -(1-\beta)\lambda\delta U_{i+1} - \bar{g}((U_{i+1}-U_i)/\delta)$. The discrete BVP, given below, has Dirichlet boundary conditions;

$$X_{n+1} = \phi^\beta(X_n) \text{ for } n = 0, 1, \ldots, N-1, \quad X_0 = \begin{pmatrix} 0 \\ W_0 \end{pmatrix}, \quad X_N = \begin{pmatrix} 0 \\ W_N \end{pmatrix}. \tag{3.2}$$

The choice of β depends on the physical boundary conditions required. We have to match the physical boundary conditions (i.e. resolve forces at each end of the lattice) with the boundary conditions that arise from requiring $S_\beta(\mathbf{U})$ to be stationary and the resulting BVP formulation (details in [9]). We have chosen fixed boundary conditions at both ends and so are free to choose any $\beta \in [0,1]$, but we notice that the map ϕ is self adjoint if we choose $\beta = \frac{1}{2}$ (i.e. $\phi_{-\delta}^{\frac{1}{2}} \circ \phi_\delta^{\frac{1}{2}} = \text{i.d.}$). This extra symmetry is useful and so we, from this point on, consider $\phi^{\frac{1}{2}}$ and call this map simply ϕ.

Before we consider the discrete BVP (3.2) we consider its continuum limit as a continuous BVP. The map ϕ is a second order symmetric and symplectic discretisation, with step length $\delta > 0$, of the Hamiltonian differential equation

$$u'' + \lambda u(1-u'^2)^{\frac{3}{2}} = 0 \tag{3.3}$$

with Hamiltonian

$$H(u,w) = -\sqrt{1+w^2} - \frac{\lambda}{2}u^2$$

where $w = u'/\sqrt{1-u'^2}$. This discretisation is a composition method formed from two steps of length $\delta/2$. The second step is a step of the symplectic Euler (SE) method and the first step is a step of the SE's adjoint method.[1] With the Dirichlet boundary conditions $u(0) = u(1) = 0$ we see this as the continuum limit of the discrete BVP (3.2). To solve this BVP we first consider the

[1] Alternatively we can see this method as a partitioned Runge-Kutta method (see [10, p25,p34]) with coefficients

1/2	0	1/2	1/2	1/2	0
1/2	0	1/2	1/2	1/2	0
	1/2	1/2		1/2	1/2

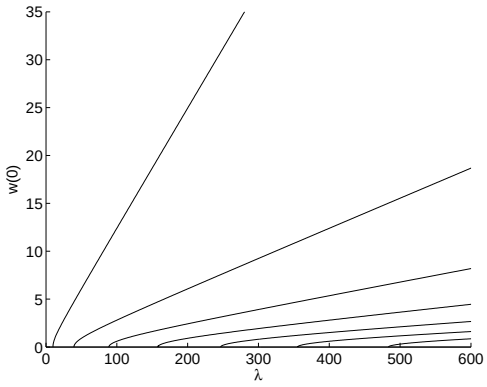

FIG. 3.1. *The bifurcation diagram for the continuous boundary value problem defined in the text from the differential equation (3.3).*

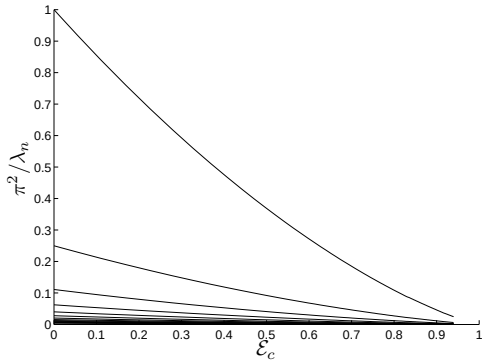

FIG. 3.2. *This shows the end-shortening load behaviour of the solution branches to the continuous BVP shown in Figure 3.1.*

differential equation (3.3) as an IVP with initial conditions $u(0) = 0$ and $u'(0) = u'_0$. This IVP has periodic solutions for all u'_0 with period given by

$$T(u'_0) = 2\sqrt{\frac{8}{\lambda(E+1)}}\,[K(k) - (E+1)E(k)]$$

where $E = (1-(u'_0)^2)^{-1/2}$, $k^2 = (E-1)/(E+1)$, $K(k)$ and $E(k)$ are the complete elliptic integrals of the first and second kinds respectively. To determine the solutions to the corresponding BVP we use the fact that a scaling symmetry of (3.3) tells us that if we have a branch of BVP solutions given by $(W_1(\lambda), \lambda)$ there are an infinite number of other branches given by $(W_1(\lambda), n^2\lambda)$ for $n \in \mathbb{N}$. Also we have that the function $T(u'_0)$ increases monotonically and so the only solutions to this BVP are solutions to (3.3) that start and finish on the u' axis in the phase space of (3.3). These facts enable us to plot the bifurcation diagram for this continuous BVP which is shown in Figure 3.1 and is useful for comparisons with the discrete BVP bifurcation diagrams that are described in the next section. Figure 3.2 shows how the nondimensional load $p = \pi^2/\lambda^2$ falls as the continuous end shortening,

$$\mathcal{E}_c = 1 - \int_0^1 \sqrt{1-(u')^2}\,\mathrm{d}x, \tag{3.4}$$

increases for the solutions on the branches shown in Figure 3.1.

3.1. Discrete BVP Behaviour. We can determine the solutions to the discrete BVP (3.2) numerically (as in [7]) using a bisection algorithm. Since the solutions to the initial value problem corresponding to the BVP (3.2) are unique each BVP solution is uniquely parametrised by W_0. Choosing an interval for W_0 in which to search and breaking this interval into segments of length ΔW_0 we look for sign changes in U_N. Once a sign change has been found a suitable zero finding algorithm can be used to approximate the value of W_0 at which $U_N = 0$. We then reduce ΔW_0 until no further solutions are found. The results of this computation for $N = 5$ and $N = 16$ are shown in figures 3.3 and 3.4 respectively. Computing the entire solution for each of these W_0 values

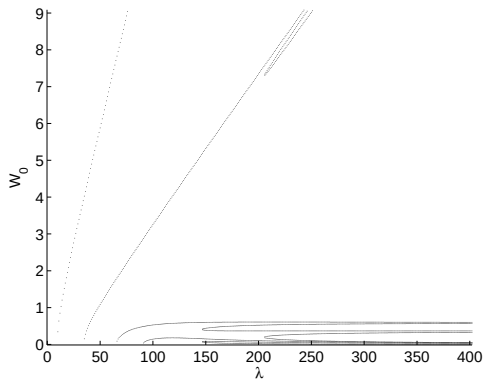

FIG. 3.3. *The bifurcation diagram for the $N = 5$ discrete boundary value problem (3.2). Note the fixed point at the origin of the map ϕ (see (3.2)) is elliptic for $\lambda > 4/\delta^2 = 125$.*

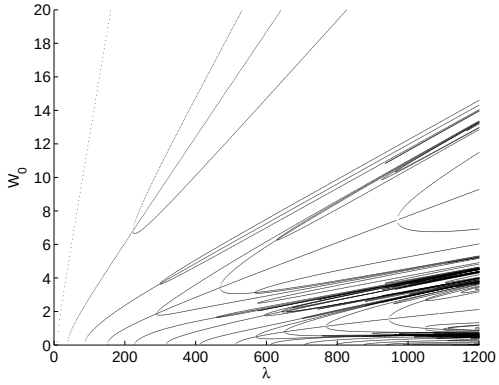

FIG. 3.4. *The bifurcation diagram for the $N = 16$ discrete boundary value problem (3.2). Note the fixed point at the origin of the map ϕ (see (3.2)) is elliptic for $\lambda > 4/\delta^2 = 1024$.*

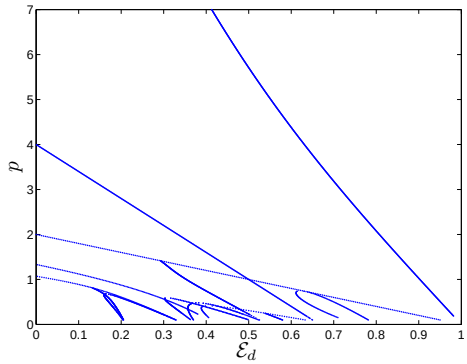

FIG. 3.5. *The solution branches of the discrete BVP (3.2) shown in Figure 3.3 showing p as a function of the end shortening $\mathcal{E}_d$.*

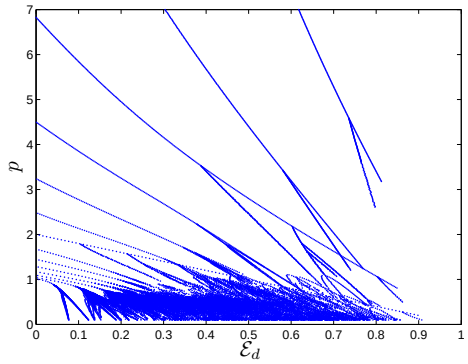

FIG. 3.6. *The solution branches of the discrete BVP (3.2) shown in Figure 3.4 showing p as a function of the end shortening $\mathcal{E}_d$.*

then allows the computation of the end shortening $\mathcal{E}_d$ for particular static equilibrium state at a particular load. Where $\mathcal{E}_d$ is a rescaled version of (2.1) given by

$$\mathcal{E}_d = \sum_{i=0}^{N-1} \left(1 - \sqrt{1 - \left(\frac{U_{i+1} - U_i}{\delta} \right)^2} \right).$$

We can then consider solutions for which $\mathcal{E}_d$ is prescribed and p is to be determined. Solutions are not unique in $(\mathcal{E}_d, p)$ space but these diagrams help us to determine which solutions we are more likely to observe in an experiment. Figures 3.5 and 3.6 show these versions of the bifurcation diagrams in 3.3 and 3.4 giving p as a function of $\mathcal{E}_d$ along each solution branch.

Solutions to the BVP (3.2) are created by one of three mechanisms.[7]

(i) Pitchfork bifurcations on the zero solution branch arising when the eigenvalues of $\phi'(0)$ move through the roots of unity, and by analogous behaviour of the map ϕ for bifurcations on the non-zero branches. These can in principle occur at any λ value.

(ii) Fold bifurcations seen towards the bottom right of figures 3.3 and 3.4 which are caused by a homoclinic tangle that appears in the phase space of the map ϕ for $\lambda > 4/\delta^2$ (see below and [11]).

(iii) Fold bifurcations which can occur for $\lambda < 4/\delta^2$, for instance $(\lambda, W_0) \approx (900, 9)$ in Figure 3.4. It is suggested in [7] that these are due to tangling of the stable and unstable manifolds of non-zero hyperbolic higher period fixed points of the iterated map ϕ.

Note that the critical transition at $\lambda \geq 4/\delta^2$ corresponds in the original variables to taking $h \geq 4P/k$ as described in the introduction. The first two of these mechanisms can be understood further by considering the linearisation of the map ϕ about the origin: $\phi'(0)$. This linearisation matrix has characteristic polynomial $P(\mu) = \mu^2 + \mu(\delta^2\lambda - 2) + 1$ and the discriminant of $P(\mu)$ tells us that the zero fixed point of ϕ is hyperbolic for $\lambda < 0$ and $\lambda > 4/\delta^2$ and elliptic for $0 < \lambda < 4/\delta^2$. As the eigenvalues of $\phi'(0)$ pass through the roots of unity as λ increases from zero to $\frac{4}{\delta^2}$ there are $N-1$ primary bifurcations from the zero equilibrium. These bifurcate at the λ values $\lambda = \lambda^*_{n,N}$ with bifurcating solutions $U_i^{(n)}$ for $i = 0, \ldots, N$ given by

$$\lambda^*_{n,N} = \frac{2}{\delta^2}(1 - \cos\frac{n\pi}{N}) \tag{3.5}$$
$$U_i^{(n)} = \pm\epsilon \sin\frac{ni\pi}{N}.$$

We can see in Figure 3.4 that there are secondary bifurcations on these primary branches. In fact, by considering the eigenvalues of ϕ' on this branch we can show [9] that for N even, on the $n = N/2$ primary branch we expect $N/2 - 1$ secondary bifurcations at the λ values

$$\lambda^{(2)}_{k,N} = \frac{4}{\delta^4(1 - \cos\frac{k\pi}{N})} \text{ for } k = 1, 2, \ldots, \frac{N}{2} - 1.$$

In the system studied in [7] tertiary bifurcations on the secondary branches were predicted but not observed. We can see from Figure 3.4 that in the system studied here there are indeed further bifurcations on the secondary branches.

When performing experiments on structural systems it is generally more common and safer to attempt to control the end shortening (equation (3.4)) of the system rather than the applied load (see [19, p188-194] for a general discussion of dead, rigid and semi-rigid loading devices). Figures 3.5 and 3.6 show how the end shortening of the static equilibrium solutions depends on the nondimensional load applied to the system (recall $p \propto 1/\lambda$). All of the static equilibrium states shown in figures 3.3 and 3.4, except the zero equilibrium for $\lambda > \lambda^*_{N-1,N}$, are dynamically unstable under controlled load (see §4) but controlling the end shortening may have a stabilising effect on some of these solutions[20]. Also, the global potential energy minimum for the system will be the state with the minimum load for a given end shortening. We then see that the physically important solutions in the huge mass of solutions shown in figures 3.5 and 3.6 are the lowest load solutions for a given end-shortening.

We thus predict an experimental scenario that unfolds via an initial distributed buckle pattern close to $p = 1$ shown in (a) of Figure 3.7. Then via secondary bifurcations this primary shape becomes asymmetric; (b) of Figure 3.7. Through further bifurcations and increased load the displacement eventually localises at the end of the structure in a spatially localised mode (c) of 3.7.

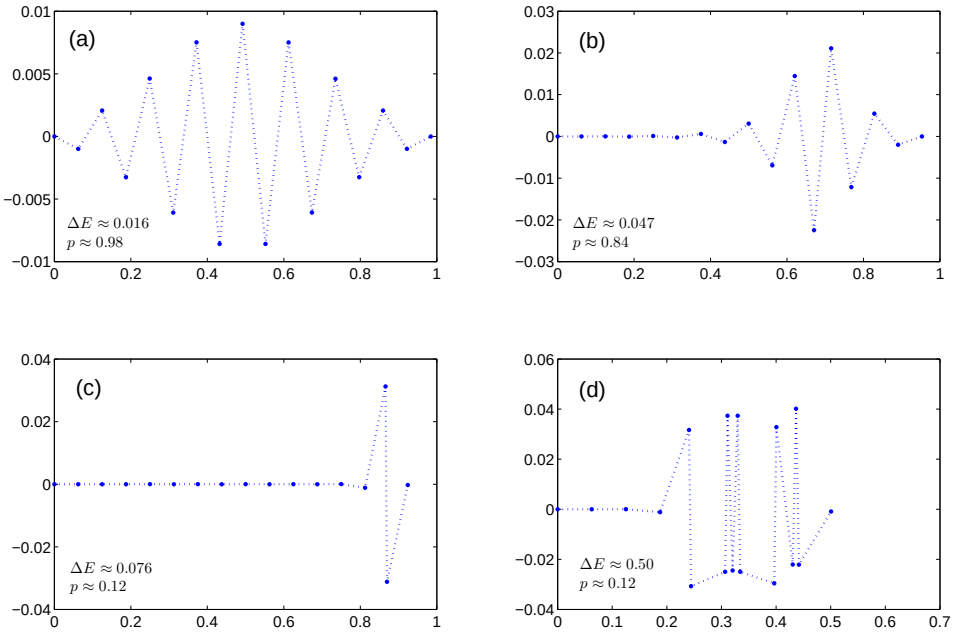

FIG. 3.7. *Evolution of the static equilibrium states of the mechanical lattice of Figure 1.1 under increasing end shortening for small to moderate end shortening (a)-(c). (d) shows a spatially irregular state for a higher value of the lattice end shortening.*

As the end shortening is increased from here we expect a jump to a child solution of the second primary branch before the chaos seen for larger end shortening values will dictate the behaviour making predicting experimental behaviour impossible. We do however expect the structure to move into spatially irregular states, an example of which is shown in panel (d) of Figure 3.7. This behaviour differs considerably from the continuum limit of this system. From Figure 3.2 we see that the branches bifurcate at loads approaching zero and the scaling argument of the previous section can tell us that solution with the lowest load for a given end shortening will be composed of infinitely many infinitely small wrinkles. This singular behaviour is due to the lack of bending stiffness in the continuum model. In reality a continuous medium will have a finite bending stiffness giving a non-zero lowest buckling load. [12]

In the next section we consider the dynamic stability of the static equilibrium states analysed in this section.

4. Stability of the Static Equilibrium States. In this section we analyse the linear stability under fixed load p of the static equilibrium states found in the previous section. We do this by monitoring the eigenvalues of $\mathbf{F}'(\mathbf{X})$ (given by (2.7)) along a branch of solutions $\mathbf{X}(\lambda)$. Before we consider all of the branches we determine the eigenvalue behaviour for the zero equilibrium analytically. We can use results of the eigenvalues of tridiagonal matrices [21], to find the eigenvalues

of $\mathbf{f}'(\mathbf{0})$. The block form of $\mathbf{F}'(\mathbf{X})$ then gives the eigenvalues

$$\begin{aligned} \gamma_k &= +\sqrt{\lambda^*_{k,N} - \lambda} \\ \gamma_{k+N-1} &= -\sqrt{\lambda^*_{k,N} - \lambda} \end{aligned} \tag{4.1}$$

for $k \in \{1, \ldots, N-1\}$ with $\lambda^*_{k,N}$ given by (3.5). These tell us that for $\lambda < \lambda^*_{1,N}$ the zero equilibrium is hyperbolic and as λ moves through each of the bifurcation points at $\lambda^*_{n,N}$ two eigenvalues with opposite sign move off the real axis, through zero, and onto the imaginary axis. The zero equilibrium is thus elliptic and linearly stable for $\lambda > \lambda^*_{N-1,N}$.

We determine the stability of the non-zero equilibria numerically. Figure 4.1 shows the number of eigenvalues of $\mathbf{F}'(\mathbf{X})$ with non-positive real parts, for $N = 8$ computed using the continuation software AUTO [5]. This figure and the enlarged inset show only the branches that are connected to the zero equilibrium. With $N = 8$ we know that for an equilibrium state to be linearly stable we require $N_s = 2(N-1) = 14$. Thus all the primary branches are unstable to varying degrees and loose stability at the secondary bifurcations, the secondary branches inheriting the stability of the primary branch. Along the secondary branches we have the opposite behaviour at the tertiary bifurcations; the secondary branch gains stability and the bifurcating solutions are less stable than the secondary branch. If this alternating behaviour of the bifurcation character continues for all branch sub-bifurcations it tells us that none of the branches connected to a primary branch can have a stability greater than that of the primary branch telling us also that all of the connected branches are linearly unstable.

Figure 4.2 shows the stability of some of the disconnected static equilibrium states for $N = 6$. The circles are solutions computed by the bisection algorithm of [7] used in §3 while the solid lines are the branches computed using the continuation software AUTO on which the stability values have been calculated. We can see that in Figure 4.2 the lower half of the disconnected branches have lower N_s than the upper branches and since with $N = 6$ we require $N_s = 10$ to have a linearly stable equilibrium there are none found in this bifurcation diagram. This circumstantial evidence leads us to conjecture that the zero equilibrium for $\lambda > \lambda^*_{N-1,N}$ is the only linearly stable equilibrium state for this mechanical system. This contrasts with the mechanical system studied in [7] where infinitely many stable solutions are found as a control parameter tends to infinity [6].

5. Breathers. Discrete breathers are time periodic solutions (with temporal frequency ω_b) to the equations of motion for a lattice with large N that are usually exponentially localised in space. There has been a large amount of work related to this phenomenon (for a reviews see [8, 1, 2]) but few of the applications have been in macroscopic engineering systems. In this section we show, using the numerical method of [16] we can find discrete breathers in the mechanical system considered in earlier sections where N is not large (e.g. $N = 16$ and $N = 29$). Furthermore, we demonstrate that in this system these breathers can be linearly stable and so potentially observable in an experiment. For convenience we rewrite the equations of motion for the lattice (2.7) in the slightly different form

$$\ddot{U}_i = -\lambda U_i - \frac{1}{\delta}\bar{g}\left(\frac{U_{i+1} - U_i}{\delta}\right) + \frac{1}{\delta}\bar{g}\left(\frac{U_i - U_{i-1}}{\delta}\right) \tag{5.1}$$

for $i = 1, \ldots, N-1$ with $U_0 = U_N = 0$ and $\bar{g}(x) = x/\sqrt{1-x^2}$.

The numerical method of [16] relies on the existence of a nonlinear anti-continuous limit of the lattice equation in question. This is a limit of one of the parameters such that in this limit the

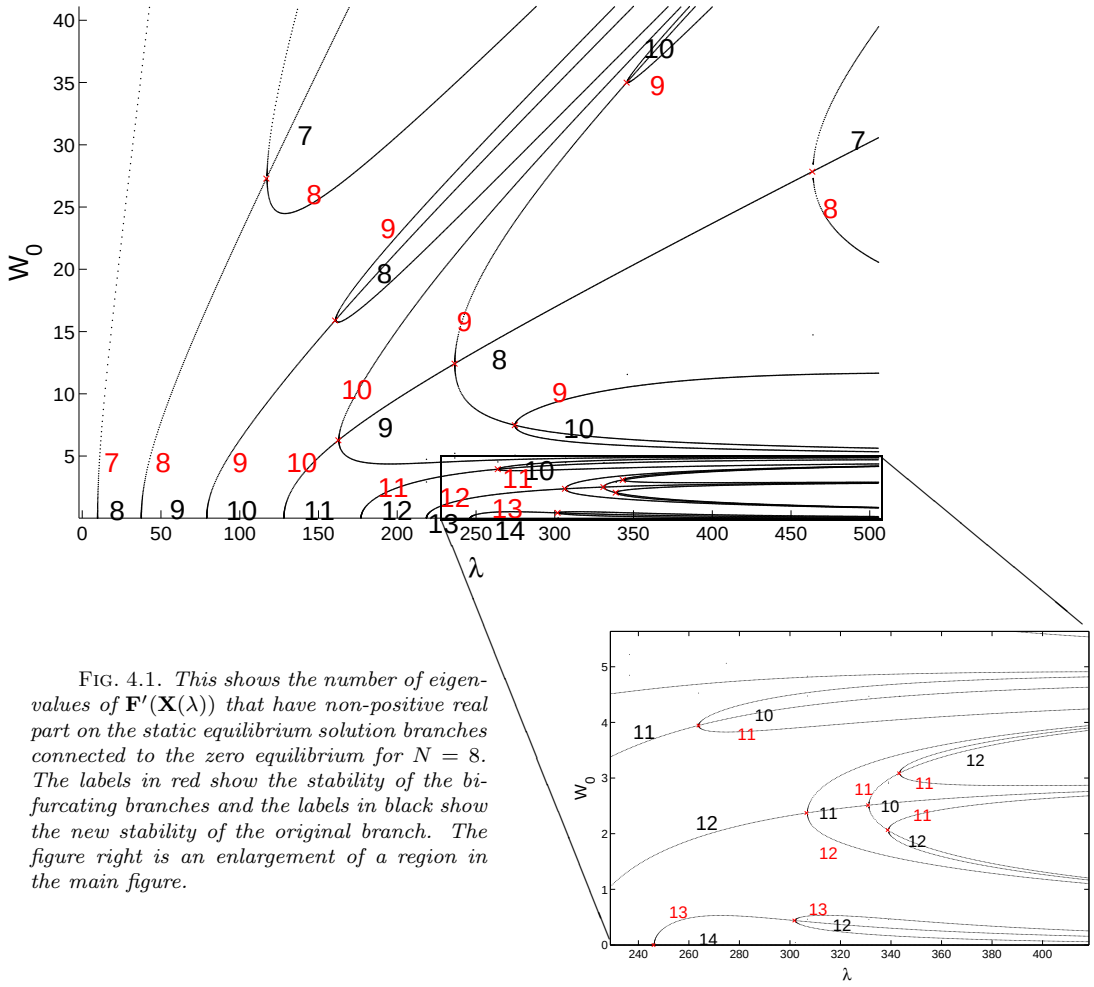

FIG. 4.1. *This shows the number of eigenvalues of* $\mathbf{F}'(\mathbf{X}(\lambda))$ *that have non-positive real part on the static equilibrium solution branches connected to the zero equilibrium for* $N = 8$. *The labels in red show the stability of the bifurcating branches and the labels in black show the new stability of the original branch. The figure right is an enlargement of a region in the main figure.*

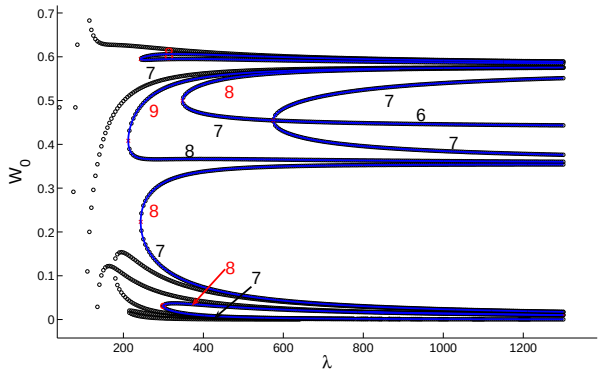

FIG. 4.2. *This shows the number of eigenvalues of* $\mathbf{F}'(\mathbf{X}(\lambda))$ *that have non-positive real part on some of the disconnected static equilibrium solution branches for* $N = 6$.

equation becomes $N-1$ decoupled *nonlinear* oscillators. A trivial breather can be created in this limit: one oscillator oscillating while the others are stationary. This breather can then be continued from the anti-continuous limit to the finite coupling regime to give the required breather. In (5.1) we see that there is no such limit and so a change of variables is required [16] to create a system that will give us breathers via the above method. This change of variables is given by

$$Y_i = U_i - U_{i-1} \tag{5.2}$$

for $i = 1, 2, \ldots, N-1$ and subtracting (5.1) for $i = j$ from (5.1) for $i = j-1$ we get the following ODE system for Y_j

$$\ddot{Y}_j = -\lambda Y_j + \frac{2}{\delta}\bar{g}\left(\frac{Y_j}{\delta}\right) - \frac{1}{\delta}\left(\bar{g}\left(\frac{Y_{j+1}}{\delta}\right) + \bar{g}\left(\frac{Y_{j-1}}{\delta}\right)\right).$$

The boundary condition $U_N = 0$ then becomes $\sum_{i=1}^{N} Y_i = 0$ while the boundary condition $U_0 = 0$ is automatically satisfied by the inverse of (5.2): $U_n = \sum_{i=1}^{n} Y_i$ for $n \geq 1$, $U_0 = 0$. At this point no progress seems to have been made, there is still no anti-continuous limit which we may use, but this can be rectified by artificially introducing another continuation parameter $C \in [0, 1]$

$$\ddot{Y}_i = -\lambda Y_i + \frac{2}{\delta}\bar{g}\left(\frac{Y_i}{\delta}\right) - \frac{C}{\delta}\left(\bar{g}\left(\frac{Y_{i+1}}{\delta}\right) + \bar{g}\left(\frac{Y_{i-1}}{\delta}\right)\right). \tag{5.3}$$

We can see now that when $C = 0$ this becomes a system of decoupled nonlinear oscillators with the softening nonlinearity $\bar{g}$. Before we produce trivial breathers in this lattice at $C = 0$ and continue these numerically up to $C = 1$ we need to investigate the behaviour of the linear solutions of this equation so that we can search for breather solutions in the appropriate part of parameter space.

5.1. The Lattice's Linear Spectrum. A necessary condition for breather solutions to exist [8] is that the the breather frequency ω_b must not resonate with the linear spectrum of the lattice. This condition prevents energy in the breather immediately transferring to the linear modes and thus destroying the spatial localisation. To determine in which parameter ranges there is no such resonance and hence we can search for breathers, we now determine the linear-spectrum of the lattice (5.3). If we linearise (5.3) we get

$$\ddot{Y}_i = \left(\frac{2}{\delta^2} - \lambda\right) Y_i - \frac{C}{\delta^2}(Y_{i+1} + Y_{i-1}) \tag{5.4}$$

which has doubly-periodic solutions

$$Y_j(t) = \cos\left(\frac{n\pi}{N}(j - \tfrac{1}{2})\right)\cos\omega t \tag{5.5}$$

for $j = 1, \ldots, N-1$, $n = 1, 2, \ldots, N-1$ that satisfy the required boundary conditions. Substituting (5.5) into (5.4) and simplifying we find that the spectrum is given by $\omega \in \{\omega_1, \ldots, \omega_{N-1}\}$ where ω_n satisfies the dispersion relation

$$\omega_n^2 = \lambda - \frac{2}{\delta^2}\left(1 - C\cos k_n\right). \tag{5.6}$$

This gives the frequency dependence of the $N-1$ linear solutions labelled by k_n where $k_n = n\pi/N$. As N is increased this set of frequencies forms a band (the phonon band) that becomes dense as

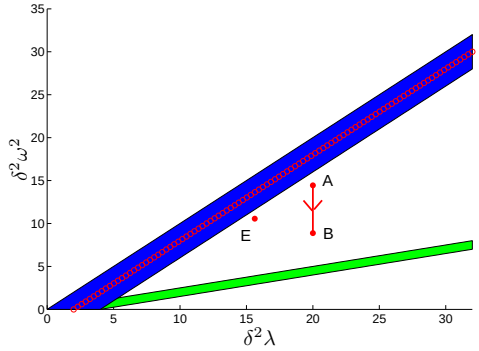

FIG. 5.1. *The phonon band width of the breather model (5.3) for $C = 1$ (blue) and band half-multiple (green). The red circles show where the spectrum collapses at $C = 0$. The vertical arrow shows the continuation path used in §6. Whilst A, B and E mark the parameter space locations of the breathers and phonobreathers found in §5 and §6.*

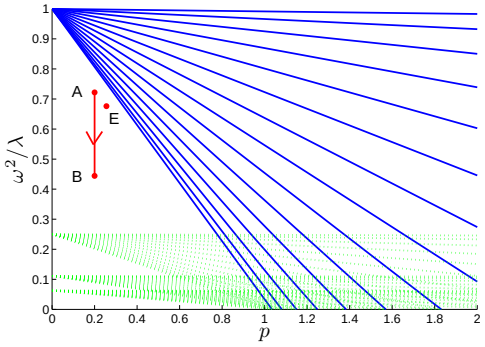

FIG. 5.2. *Frequency dependence of each of the linear solutions on the lattice (5.5) in the particular case $N = 16$ (in blue). The lines in red are points in parameter space for which $n\omega_b = \omega_i$ where ω_i is the frequency of the ith linear mode. A, B and E mark the points that correspond to A, B and E in Figure 5.1.*

$N \to \infty$. The blue (upper) band of Figure 5.1 shows how the width of this band (at $C = 1$) varies as the load parameter $\lambda \propto 1/p$ is varied. The green (lower) region is the set of frequencies $\omega_n/2$ for ω_n inside the phonon band. Breathers potentially exist for values between the blue and green bands. At $C = 0$ the oscillators are decoupled and all oscillate at the same the same frequency given by the red circles. Figure 5.2 shows the spread of the 15 normal mode frequencies (solid lines) for $N = 16$ and how they vary as the nondimensional load parameter p is varied, along with the dotted lines plotted at a half, third and quarter of the mode frequencies.

5.2. A Stable Breather Solution. The decoupled ($C = 0$) nonlinear oscillators of (5.3) are of softening type (the frequency decreases with amplitude) and so we can only find sub-band breathers. We are now in a position to use numerical continuation software such as AUTO[5] to follow the solution branch in C at constant ω and λ.

Figure 5.3 shows a result of this computation and is the solution at $C = 1$ continued from the phase sequence [0000000100000000] for $N = 16$, $\lambda = 4000$ at the anticontinuous limit $C = 0$. The inset shows the exponential decay of the tails and the solution approximately satisfies $\sum_{i=1}^{N} Y_i = 0$ which demonstrates the ability of the mechanical system to exhibit breather solutions. To link this with the work of §4 we see from the bifurcation diagram of the static equilibrium states (Figure 3.4) that $\lambda = 4000$ is well into the parameter region where the dynamic phase space has a complicated and tangled structure due to the multitude of static equilibrium states shown. Figure 5.4 shows the result of a similar continuation for the lattice with $N = 29$ but this time the breather solution has been transformed back into the original lattice coordinates of equation (5.1).

We have determined, numerically, that at least two breather solutions exists in the mechanical system of Figure 1.1 but in order to observe a breather experimentally we require the solution to be at least linearly stable. The linear stability of a solution found previously can be determined by computing the characteristic multipliers (eigenvalues) μ_i for $i = 1, 2, \ldots, 2(N-1)$ of the Floquet matrix for the solution. For the period τ solution $\mathbf{Y}(t)$ the eigenvalues of this matrix give the eigenvalues of the map $Y(0) \to Y(\tau)$. If all these eigenvalues lie on the unit circle in the complex

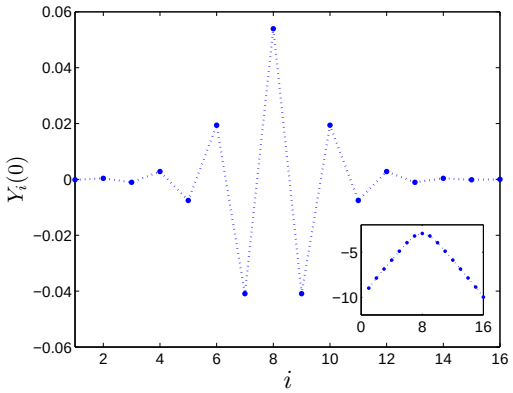

FIG. 5.3. *Spatial profile at maximum amplitude of a breather solution at point E in figures 5.1 and 5.2 ($N = 16$, $\lambda = 4000$, $\omega = 52$). This breather is found in the lattice (5.3), at $C = 1$ continued by continuing from the phase sequence* [0000000100000000] *at $C = 0$. The inset is a graph of* $\log(|Y_i(0)|)$ *and clearly demonstrates the exponential spatial decay of the breather tails.*

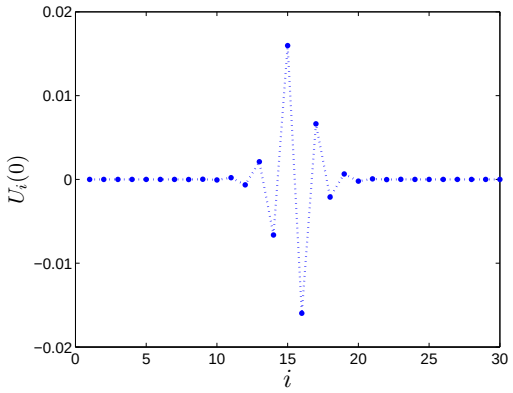

FIG. 5.4. *This shows an antisymmetric breather solution in the original lattice coordinates of equation (5.3) at point A in figures 5.1 and 5.2 ($\lambda = 16820$,$N = 29$,$\omega = 110.2$). This was continued from the phase sequence* $[0 \ldots 00100 \ldots 0]$ *at $C = 0$ in the transformed lattice (5.3).*

plane and are distinct then the periodic solution is linearly stable.

Figure 5.5 gives the location of the eigenvalues μ_i for $i = 1, \ldots, 2(N-1)$ of the Floquet matrix for the breather solution with $N = 29$ shown in Figure 5.4. All of the eigenvalues $\mu_n = r_n \exp(i\theta_n)$, at least to within numerical precision, appear to lie on the unit circle ($\max_n(r_n) - \min_n(r_n) \approx 1.5 \times 10^{-6}$) and are distinct ($\min_{n \neq m} |\theta_n - \theta_m| \approx 1.2 \times 10^{-3} \approx 0.43^\circ$) and so the breather solution is linearly stable.

With this knowledge we can then ask: how long do we expect system to stay 'near' a breather solution. A partial answer to this question is shown in Figure 5.6. This shows the result of a time integration of the equations of motion for the lattice (5.1) with $N = 29$ starting near the initial conditions required for the exact periodic breather solution illustrated in Figure 5.4 ($U(0) = 0.98U_0$ where U_0 is a point of maximum amplitude for the exact breather solution). From this computation we can see that the breather solution is quite stable nonlinearly as well as linearly. Over roughly 20 breather periods energy starts to leak into the tails but this does not immediately destroy the high amplitude breather core and after 50 breather periods the tail amplitude has grown to only 20% of the original breather core amplitude.

6. Phonobreathers. Here we continue (using AUTO[5]) the breather solution of Figure 5.4 from point A of figures 5.1 and 5.2 down the red, arrowed line to point B by keeping λ fixed and decreasing ω. At point B the breather frequency ω_b satisfies $\omega_b = \frac{2}{3}\omega_1$ (numerically this condition was satisfied with a relative error of $1.5 \times 10^{-5}\%$) where w_{p_1} is the frequency of the highest frequency phonon. Also at point B, AUTO reports that another branch of solution intersects with this breather branch. This bifurcation scenario is shown in Figure 5.7 where $\|\mathbf{U}\|$ denotes the solution norm given by

$$\|\mathbf{U}\| = \sqrt{\int_0^1 \sum_{k=1}^{N-1} U_k(t)^2 \, \mathrm{d}t}.$$

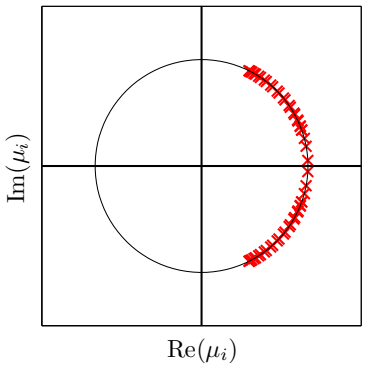

FIG. 5.5. *Eigenvalues of the Floquet matrix for the $N = 29$ breather solution found in §5.2 relative to the unit circle in the complex plane.*

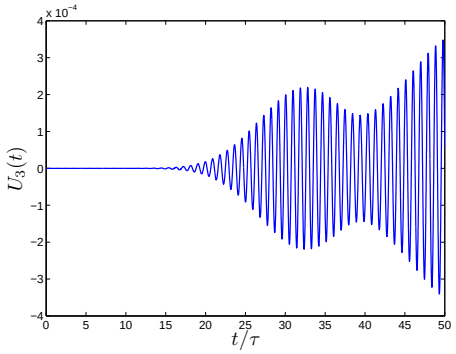

FIG. 5.6. *The time evolution $U_3(t)$ for the lattice equations (5.1) for an initial condition close to a breather solution $U(0) = 0.98U_0$ where U_0 is the phase space position of the exact breather solution at maximum amplitude. The breather period is $\tau = 2\pi/\omega_b$.*

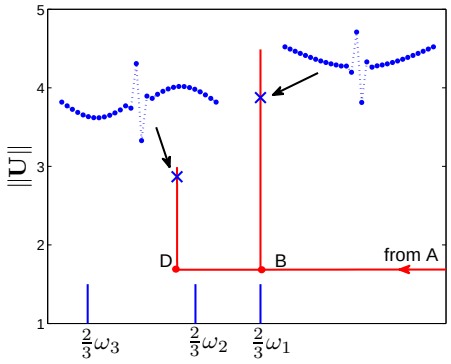

FIG. 5.7. *Diagram showing the bifurcation of two phonobreather solutions from the branch of breather solutions given by the vertical arrowed line in Figure 5.1. the lower, vertical, blue lines show $2\omega_i/3$ for $i = 1, 2, 3$.*

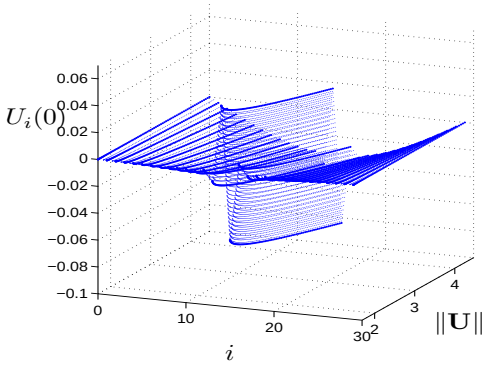

FIG. 5.8. *This shows the evolution of the phonobreather solutions up the branch starting at B in Figure 5.7.*

If we then switch onto this branch we can see in Figure 5.8 that as we move along the new branch the tails of the breather grow in amplitude in a spatial pattern that is the similar to the highest frequency linear mode. We also find that on this branch the frequency of the new solution is half that of the original breather solution, and so this is a bifurcation in which the period doubles. This type of solution is known as a phonobreather solution [18, 16] and we believe that this is the first observation of a phonobreather solution in a mechanical lattice system.

If we continue to follow the main breather branch further, towards lower frequencies and point D of Figure 5.7, when ω_b is near $\frac{2}{3}\omega_2$ AUTO appears to step onto another branch of phonobreather solutions with twice the period of the original breather solution. As can be seen in Figure 5.7 this

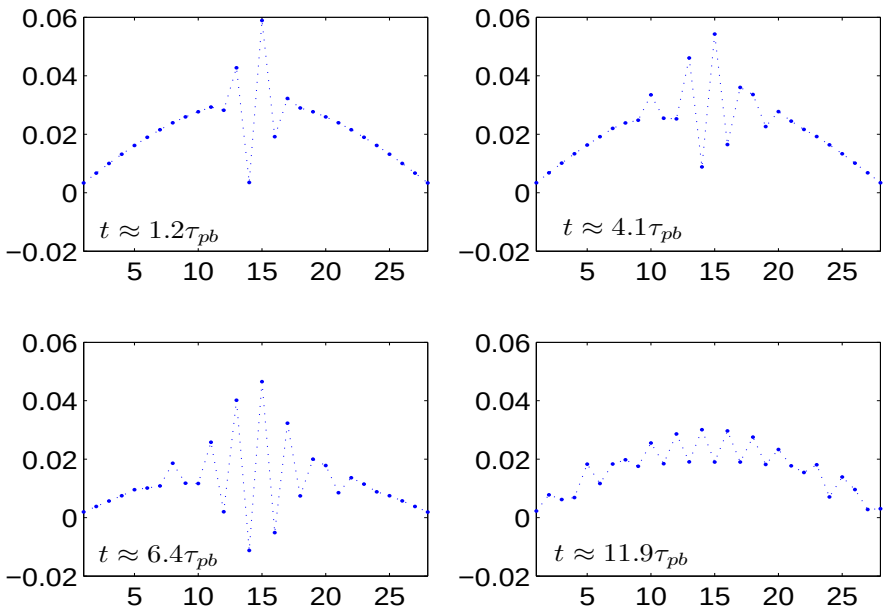

FIG. 6.1. *Snapshots of the time evolution of the lattice equation (5.1) with an initial condition close to an exact phonobreather trajectory. The temporal period of the exact phonobreather is* $\tau_p b$.

appears not to coincide exactly with ω_2 rather, it happens at a slightly lower frequency. These two apparently separate branches are extremely close and are difficult to separate numerically and so the exact bifurcation scenario at D and B is unclear and requires further careful numerical study to see if this behaviour is the same as, or different to, that presented in [18].

This raises interesting questions. Although this branch appears to be a resonance between the breather solution and the second highest frequency phonon why does this 'bifurcation' not occur at exactly the resonant frequency value? Also, on this second branch, the frequency-amplitude behaviour is the same as for the first bifurcation the frequency being essentially independent of the phonobreather tail amplitude. This is surprising as normally when continuing a linear mode in to the nonlinear regime the frequency depends heavily on the amplitude but here the core of the phonobreather appears to reduce or even prevent this change in frequency.

6.1. Phonobreather Stability. Whilst exact phonobreathers themselves appear to be very unstable, initial data close to such solutions leads to interesting dynamics which we might expect to observe experimentally. To investigate this we perform a simulation similar to that of the previous section. We start our IVP solver close to the point of peak amplitude for a phonobreather solution and then integrate forward in time. The results for this calculation on the first phonobreather found in the previous section are summarised in Figure 6.1 and can be seen in full on-line in the movie file 'pb1drift.mpg'.

The system stays very close to the exact phonobreather solution for only a short period of time (around one τ_{pb}) but the later dynamics does not head immediately into thermal equilibrium.

Qualitatively we can split the spatial profile into the breather core and nonlinear-phonon tails. The simulation shows the breather core loosing its neat compact form and the central dynamics becoming less regular. This less regular motion is only over a few lattice sites at first and then it slowly expands outwards encompassing more and more of the stable nonlinear-phonon tails. For the particular case shown in Figure 6.1 where the phonobreather tail has the same spatial wave length as the highest frequency linear mode it is interesting to note that the less regular motion that causes the breather core to grow appears to be almost entirely composed of a spatial pattern similar to the lowest frequency linear mode, suggesting that the highest and lowest frequency linear modes are more strongly coupled to each other than to the other linear modes.

We estimate the speed of this drift by looking at the time series for each of the lattice nodes in the tail. Before the phonobreather core reaches a particular lattice site labelled by i, $U_i(t)$ oscillates with constant amplitude. We say that the phonobreather core has reached a particular lattice site at time t_c^i when the amplitude of oscillation (i.e. $U_i(t)$ when $\dot{U}_i(t) = 0$) has changed by the relative amount 5×10^{-4}. This motivates the following definition of t_c^i

$$t_c^i = \{\min(t) \text{ such that } \dot{U}_i(t) = 0 \text{ and } \left|\frac{U_i(t) - U_i(0)}{U_i(0)}\right| < 5 \times 10^{-4}\}$$

and tracking the dependence of t_c^i on i gives us the speed of the phonobreather core's expansion. This is shown in Figure 6.2 for the left (a) and right (b) phonobreather tails of the dynamical system seen in Figure 6.1. From this figure we can see that the speed of this core drift seems to be constant in time i.e. the core grows linearly with time. The best fit lines in Figure 6.2 have equations

$$\text{Left:} \quad t_c^n = -0.26n + 3.16 \quad \text{Right:} \quad t_c^n = 0.24n - 4.21.$$

Since this system is symmetric about its midpoint we expect the left and right velocities to be the same and the differences are due to the nature of this approximation. Averaging the two drift velocities we get $v \approx 0.25$.

To ensure that this drift is not due to the specific numerical integrator we have used this analysis has been performed with two numerical integrators. The results just presented were calculated using Matlab's ode45 routine with abstol=1×10^{-8} and reltol= 1×10^{-6}. For comparison we have also done this analysis using a fourth order symplectic integrator [14, p147] with a step size of $\delta t \approx 6.6 \times 10^{-4}$. Although the individual trajectories from these two integrators vary slightly near the phonobreather core, the behaviour is essentially the same and the mean core edge drift velocity for the symplectic integrator is $v \approx 0.27$.

This drift property tells us that although the exact phonobreather trajectory may be unstable, close to this trajectory in phase space we see interesting dynamical behaviour that has a chance of being observed experimentally.

7. Conclusions. We have investigated some aspects of the static and dynamic behaviour of a discrete mechanical lattice. We have extended results on spatial chaos in the static equilibrium states of an infinite version of this lattice [11] and shown how these lead to a complex bifurcation structure (for sufficiently large link size) in the finite lattice similar to that seen, for a different, less structurally relevant lattice, in [7]. We have also analysed the stability of the spatially chaotic static equilibrium states and find that all but the zero equilibrium state for $\lambda > \lambda^*_{N-1,N}$ are unstable under controlled load. Physical considerations suggest that in an experiment that controls the end shortening of the lattice, a small fraction of these solutions may be observable experimentally.

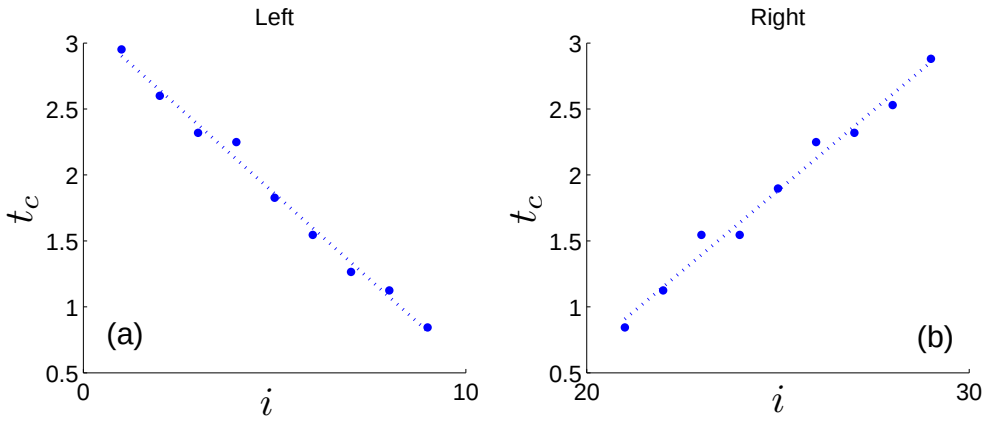

FIG. 6.2. *Dependence of t_c^i (see text for the definition) on i showing that width of the phonobreather's core grows linearly with time.*

We have also shown that this mechanical lattice can support sub phonon-band breather solutions that are linearly stable and have a lifetime in the nonlinear lattice system of at least 20 breather periods. A particular breather solution then leads onto the observation of phonobreather solutions in this nonlinear lattice.

We finally have presented new results that show that in this lattice the frequency of phonobreather solutions appears to be independent, or very weakly dependent, on their solution norm (related to the phonobreather's tail amplitude). Also these solutions may bifurcate from a path of breather solutions at frequencies in the gap between the linear spectrum and the first sub-spectrum integer resonance. Further new results on the nonlinear stability of a phonobreather solution show that over time the core of the phonobreather grows in width at a constant velocity gradually enveloping the nonlinear phonon tails. These results suggest that along with the stable breather solutions found above, phonobreather solutions and the associated dynamics could also be observed in this mechanical system experimentally.

Acknowledgements. S.C.Green would like to thank the Engineering and Physical Sciences Research Council for their support through a DTA grant.

REFERENCES

[1] S AUBRY, *Breathers in nonlinear lattices: Existence, linear stability and quantization*, Physica D, 103 (1997), pp. 201–250.

[2] ———, *Discrete breathers: Localization and transfer of energy in discrete hamiltonian nonlinear systems*, Phys. D, 216 (2006), pp. 1–30.

[3] S AUBRY, G KOPIDAKIS, AND V KADELBURG, *Variational proof for hard discrete breathers in some classes of hamiltonian dynamical systems*, Discrete Contin. Dyn. Syst. Ser. B, 1 (2001), pp. 271–298.

[4] W -J BEYN AND J LORENZ, *Spurious solutions for discrete superlinear boundary value problems*, Computing, 28 (1981), pp. 43–51.

[5] E J DOEDEL, A R CHAMPNEYS, T F FAIRGRIEVE, YU A KUZNETSOV, B SANDSTEDE, AND X WANG, *Auto97: Continuation and bifurcation software for ordinary differential equations (with homcont)*. Technical Report, Concordia University, 1997.

[6] Gábor Domokos, *Static solitary waves as limits of discretization: a plausible argument*, Phil. Trans. R. Soc. Lond. A, 355 (1997), pp. 2099–2116.
[7] G Domokos and P Holmes, *Euler's problem, euler's method, and the standard map; or, the discrete charm of buckling*, J. Nonlinear Sci., 3 (1993), pp. 109–151.
[8] S Flach and C R Willis, *Discrete breathers*, Phys. Rep., 295 (1998), pp. 181–264.
[9] S C Green, *The statics and dynamics of mechanical lattices.* PhD thesis, in preparation, University of Bath.
[10] E Hairer, C Lubich, and G Wanner, *Geometric Numerical Integration*, Springer Series in Computational Mathematics, Springer, 2002.
[11] Giles W Hunt, R Lawther, and P Providencia E Costa, *Finite element modelling of spatially chaotic structures*, Internat. J. Numer. Methods Engrg., 40 (1997), pp. 2237–2256.
[12] Giles W Hunt, Mark A Peletier, Alan R Champneys, Patrick D Woods, M Ahmer Wadee, Chris J Budd, and Gabriel Lord, *Cellular buckling in long structures*, Nonlinear Dynamics, 21 (2000), pp. 3–29.
[13] G James, *Centre manifold reduction for quasilinear discrete systems*, J. Nonlinear Sci., 13 (2003), pp. 27–63.
[14] Benedict Leimkuhler and Sabastian Reich, *Simulating Hamiltonian Dynamics*, vol. 14 of Cambridge Monographs on Applied and Computational Mathematics, Cambridge University Press, 2004.
[15] R S MacKay and S Aubry, *Proof of existence of breathers for time-reversible or hamiltonian networks of weakly coupled oscillators*, Nonlinearity, 7 (1994), pp. 1623–1643.
[16] J L Marin and S Aubry, *Breathers in nonlinear lattices: numerical calculation from the anticontinuous limit*, Nonlinearity, 9 (1996), pp. 1501–1528.
[17] J E Marsden and M West, *Discrete mechanics and variational integrators*, Acta Numer., (2001), pp. 357–514.
[18] Anna Maria Morgante, Magnus Johansson, Serge Aubry, and Georgios Kopidakis, *Breather-phonon resonances in finite-size lattices: 'phantom breathers'?*, J. Phys. A: Math. Gen., 35 (2002), pp. 4999–5021.
[19] J M T Thompson and G W Hunt, *Elastic instability phenomena*, Wiley-Interscience publication, Wiley, 1984.
[20] J M T Thompson and G W Hunt, *A General Theory of Elastic Stability*, Wiley, London, 1973.
[21] Yueh Wen-Chyuan, *Eigenvalues of several tridiagonal matrices*, Appl. Math. E-Notes, 5 (2005), pp. 66–74.